




## Open Archive Toulouse Archive Ouverte (OATAO)

OATAO is an open access repository that collects the work of Toulouse researchers and makes it freely available over the web where possible

This is a Publisher's version published in: <http://oatao.univ-toulouse.fr/27592>

**Official URL:** <https://doi.org/10.1016/J.JMRT.2020.08.008>

**To cite this version:**

Regordosa, Anna and de la Torre, Urko and Sertucha, Jon and Lacaze, Jacques  *Quantitative analysis of the effect of inoculation and magnesium content on compact graphite irons — Experimental approach.* (2020) *Journal of Materials Research and Technology*, 9 (5). 11332-11343. ISSN 2238-7854

Any correspondence concerning this service should be sent to the repository administrator: [tech-oatao@listes-diff.inp-toulouse.fr](mailto:tech-oatao@listes-diff.inp-toulouse.fr)



## Original Article

# Quantitative analysis of the effect of inoculation and magnesium content on compact graphite irons — Experimental approach



Anna Regordosa<sup>a</sup>, Urko de la Torre<sup>a</sup>, Jon Sertucha<sup>a</sup>, Jacques Lacaze<sup>b,\*</sup>

<sup>a</sup> Investigación y Desarrollo de Procesos Metalúrgicos, Azterlan, Basque Research Technological Alliance, Durango, Bizkaia, Spain

<sup>b</sup> CIRIMAT, ENSIACET, Université de Toulouse, Toulouse, France

### ARTICLE INFO

#### Article history:

Received 5 February 2020

Accepted 2 August 2020

Available online 23 August 2020

#### Keywords:

Compact graphite iron

Magnesium fading

Inoculation

Solidification

Thermal analysis

### ABSTRACT

In many industrial domains, compact graphite cast irons are developing rapidly at the expense of lamellar graphite irons. The formation of the microstructure, especially graphite shape, during the solidification stage of these alloys is however still not clearly understood, showing characteristics similar to both lamellar and spheroidal graphite irons. The aim of this work was to provide quantitative information on the solidification of compact graphite cast irons, whether inoculated or not, by thermal analysis in the foundry shop. This includes the effect of the amount of nodularizer on the undercooling before solidification starts and the amount of recalescence when bulk eutectic solidification sets up. Comparing quantitative analysis of the as-cast microstructure with the characteristics of the cooling curves gives hints to a better understanding of the microstructure formation in compact graphite irons. This work thus provides a set of quantitative data necessary to verify the relevance of any solidification modelling approach for compact graphite cast iron. On a practical point of view, it suggests that thermal analysis could certainly be a useful means for control of melt preparation for CGI casting by adding very low level of inoculant in the standard thermal analysis cups.

© 2020 The Author(s). Published by Elsevier B.V. This is an open access article under the CC BY-NC-ND license (<http://creativecommons.org/licenses/by-nc-nd/4.0/>).

## 1. Introduction

Compared to lamellar graphite cast irons (LGI), compact graphite cast irons (CGI) have improved properties and are replacing them for more and more components [1]. As for other cast irons, alloying allows fine tuning of the final mechanical properties [2] mainly by modifying the matrix microstructure. Bazdar et al. [3] showed that these mechanical properties depend also on the so-called compactness

of graphite particles which they changed by sulfur addition. Nevertheless, the satisfactory production of CGI is somewhat difficult because the desired graphite distribution, i.e. a mixture of compact and spheroidal particles, is very sensitive to various process parameters. The cooling rate becomes prevalent in thin walled casting as investigated by Charoenvilaisiri et al. [4]. Also, chemical composition, and in particular the presence of minor elements such as Al, S and Ti [5–7], affects the compactness as does also the inoculation level [8]. The need for a definition of a simple testing procedure ensuring low nodularity and maximum compactness is hampered by the fact that a clear understanding of compact graphite formation is not yet available [9].

\* Corresponding author.

E-mail: [jacques.lacaze@ensiacet.fr](mailto:jacques.lacaze@ensiacet.fr) (J. Lacaze).

<https://doi.org/10.1016/j.jmrt.2020.08.008>

2238-7854/© 2020 The Author(s). Published by Elsevier B.V. This is an open access article under the CC BY-NC-ND license (<http://creativecommons.org/licenses/by-nc-nd/4.0/>).

The cheapest and most common method for producing CGI consists in using low addition of a nodularizer, which is most often an FeSiMg alloy containing rare earth additions. Checking that the amount of nodularizer in the melt is correct can be done prior to pouring by controlling the oxygen level [10] although this is not a common procedure. In fact, the recent development of CGI relies on thermal analysis [11]. Thermal analysis (TA) uses the particularity that bulk eutectic solidification of non-inoculated CGI starts at a high undercooling, which is sometimes larger [12,13] and sometimes smaller [14] than that encountered with spheroidal graphite irons (SGI). Once solidification has started, recalescence is high as for LGI unless cementite precipitates concurrently [15]. Because of these complicated features, the characteristics of the thermal records are highly scattered [16]. To overcome this problem in the use of TA for melt control, a complex procedure using a special crucible with two thermocouples has been developed by Sintercast, as indicated in Dawson [11]. An alternative was sought by Sun et al. [17] who suggested a pattern recognition based method using a database where previous records and analyses are stored.

Due to the deep undercooling before bulk eutectic solidification, CGI is inoculated. This increases nodularity in thin section castings [9]. It would thus be of interest in being able to correlate characteristic features of thermal analysis of non-inoculated CGI with final microstructure of the same alloys but inoculated. Such a correlation should be established for a variable level of nodularizer, which can be achieved by holding the melt for an increasing amount of time, as was done by Hernando et al. [18] and Jinhai et al. [13], amongst others. The present study was dedicated to the study of the effect of holding time and inoculation rate on the formation of compact graphite using an alloy held liquid for several hours in a large pressurized pouring unit. At regular intervals, two TA cups were filled with liquid and their cooling curves recorded. One of the cups contained an inoculant, the other did not. The change in cooling records and the associated evolution of the microstructure during melt holding are presented. This provides quantitative information on the effects of inoculation and nodularizer content that could later be used to validate a modelling approach or be entered into a database for melt control.

## 2. Experimental procedure

At the end of a normal production shift, 4 t of cast iron were left in the 8 t pressurized pouring unit of the Betsaide S.A.L. foundry (Basque Country, Spain) where the tests were carried out. This cast iron had been prepared for the production of spheroidal graphite castings using a FeSiMg spheroidizer containing some cerium and lanthanum [19]. Just before each pour, the pouring basin was filled twice to ensure chemical homogeneity, especially of the magnesium. Approximately every 25 min, a set of analyses was made, and a melt sample taken out from the pouring basin was used to fill two TA cups and to obtain a medal sample, which was then used to determine the chemical composition of the alloy. One of the TA cups was empty when it was filled while the other one contained 0.35 g of a commercial inoculant (grain size

0.2–0.5 mm, Si = 69.9, Al = 0.93, Ca = 1.38, Bi = 0.49, RE = 0.37 and Fe balance, wt.%), i.e. about 0.10 wt.% of the sample weight poured in the cup. Times at which sampling was carried out were controlled so as to monitor the evolution of the alloy during holding for 8 h in the press-pour. The 19 castings were identified with a letter from A to S and a subscript “no-inoc” and “inoc” for not inoculated and inoculated alloys, respectively. During holding, the temperature of the liquid metal increased so that the first temperature recorded with the thermal cup – denoted peak temperature,  $T_{peak}$  - varied from 1283 to 1367 °C. The precise values are reported with metallographic results.

The composition of the collected medals was analysed by combustion (LECO CS300) for carbon and sulfur and by spark spectrometry (SPECTROLAB) for all other elements. The initial composition (wt.%) in the main elements is listed in Table 1, which does not include the contribution of the inoculant addition; the alloy contained also <0.01 Mo, <0.01 V, <0.01 Al and <0.005 Co, and had about 0.05 Cr and 0.006 Sn. The whole set of compositions is listed in Appendix A.

During holding, the carbon and silicon contents decreased respectively to 3.65 and 2.39 wt.%, while the evolution of Mg, Ce and La was more marked. Fig. 1 presents the evolution of these five elements as normalized with the values in Table 1. The content in all other elements was unchanged during the holding time. The carbon equivalent CE of the melt was calculated by using the two following expressions,  $CE_{99}$  as described in Appendix B [20] and  $CE_{ASM}$  [21]:

$$CE_{99} = w_C + 0.28 \cdot w_{Si} + 0.007 \cdot w_{Mn} + 0.092 \cdot w_{Cu} + 0.303 \cdot w_P \quad (1)$$

$$CE_{ASM} = w_C + 0.31 \cdot w_{Si} - 0.028 \cdot w_{Mn} + 0.076 \cdot w_{Cu} + 0.331 \cdot w_P \quad (1')$$

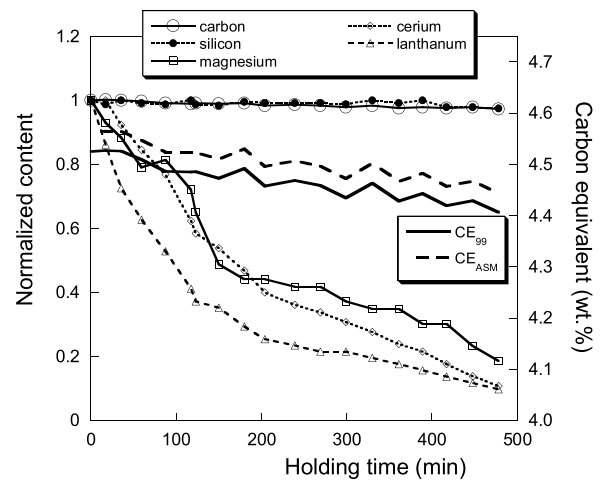


**Fig. 1 – Effect of holding time on the content of the melt in C, Si, Mg, Ce and La relative to the composition of the first sample, and of the calculated carbon equivalent CE according to the two Eqs (1) and (1’).**

**Table 1 – Chemical composition of the first medal sample (wt.%).**

C	Si	Mn	S	Cu	Mg	Ti	Ce	La
3.75	2.45	0.64	<0.005	0.85	0.043	0.021	0.0130	0.0051

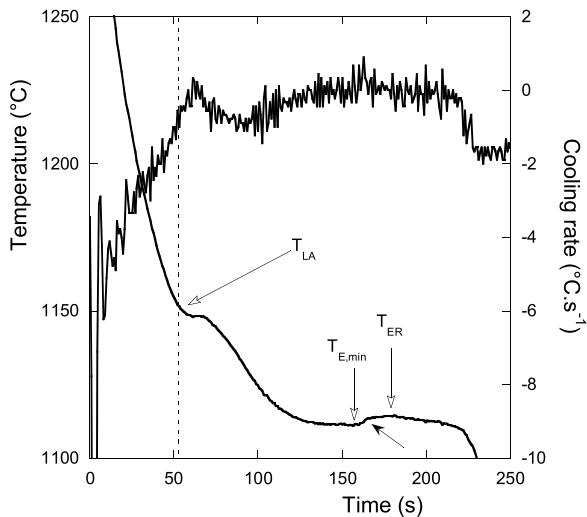


**Fig. 2 – Typical example of cooling curve and its time derivative (non-inoculated Q alloy) with definition of the characteristic temperatures (open arrows), see text. The solid arrow indicates an abrupt recalescence which is referenced to later in the main text.**

where  $w_i$  is the content in wt.% of element “i”. The two CE values are plotted in Fig. 1 where it is seen that they run parallel to each other with  $CE_{ASM}$  shifted upwards by an amount of about 0.04 wt.% C. Further comparison of these two expressions is provided in Appendix B. Both  $CE_{99}$  and  $CE_{ASM}$  decreased during the holding, though remaining above the eutectic value which means the melt remained hypereutectic all along the experiment.

The Thermolan<sup>®</sup> software was used to record the cooling curves which were then redrawn and analysed as illustrated with Fig. 2. Relevant characteristic temperatures were then evaluated, namely the maximum or peak temperature just after pouring,  $T_{peak}$ , the so-called liquidus temperature,  $T_{LA}$ , the minimum eutectic temperature,  $T_{E,min}$ , the maximum eutectic temperature during the eutectic plateau,  $T_{ER}$ , and the solidus temperature,  $T_{solidus}$ . This evaluation was made by direct reading of the cooling curve record for  $T_{peak}$ ,  $T_{E,min}$  and  $T_{ER}$ . The difference between these last two temperatures is the recalescence:  $R = T_{ER} - T_{E,min}$ . The  $T_{LA}$  temperature corresponds to the temperature at which the solidification is first sensed by the thermocouple. For hyper-eutectic alloys as those investigated here, it corresponds to the appearance of austenite after primary deposition of graphite. In practice,  $T_{LA}$  was evaluated as the temperature at which the derivative of the cooling curve shows a slope change at the end of liquid cooling. The location of this change is indicated with the dashed line in Fig. 2. In this case, which is shown, the slope change is positive, but it could as well be negative in cases where the cooling rate is close to 0 when solidification is sensed. Accordingly, the determination of  $T_{LA}$  may sometimes be inaccurate. Finally, the solidus tem-

perature was determined as corresponding to a minimum in the second derivative of the cooling curve.

The TA cup samples were then prepared for metallographic inspections. Micrographs of three different fields were taken at a magnification of  $\times 100$  in the center part of the samples, close to the thermocouple junction. The graphite distribution and shape were then evaluated with an image analysis software. The graphite particles were sorted according to the standard for spheroidal graphite, class III for irregular precipitates and class V and VI for irregular and well-shaped spheroids, respectively. In the present study, class III particles stand for compact graphite. The count (index C) and area (index A) fractions of each class were then evaluated and normalized with the total count and area of graphite, i.e. one has  $f_{III,C} + f_{V,C} + f_{VI,C} = 1$  and  $f_{III,A} + f_{V,A} + f_{VI,A} = 1$ . Nodularity could be expressed as the sum  $f_{V,C} + f_{VI,C}$ . Then, the structure of the samples was checked by etching the polished surfaces with Nital 5% to look for the presence of eutectic cementite. When carbides were observed, their area fraction ( $f_{carbides}$ ) was determined on the etched surfaces. However, for getting the proper contrast, the images were processed in such a way that ferrite in ledeburite was counted as cementite. Depending on the microstructure of the white eutectic, the fraction of carbides reported in the present work may thus as well represent the amount of white eutectic.

An attempt was carried out to characterize the size and number of the eutectic cells on metallographic sections of the non-inoculated samples after etching. In case of samples without carbides, three micrographs at  $50\times$  magnification were used and delimitation of the cells was based on identification of eutectic cells boundaries. When carbides were present, they delineated the contours of the eutectic cells which were then identified on three micrographs at  $25\times$  magnification. The maximum diameter  $D_{Cell}$  of all eutectic cells and their surface count  $N_{Cell}$  were then determined. Because the number of cells was quite low in non-inoculated samples, their size could be best represented by the average of the five largest diameter values found, which was used as  $D_{Cell}$  value.

### 3. Results

Solidification of all inoculated alloys showed a single eutectic plateau with a maximum temperature,  $T_{ER}$ , which did not change much during the holding time. This is illustrated with the records for  $A_{inoc}$  and  $S_{inoc}$  samples in Fig. 3-a where the stable,  $T_{EUT}$ , and metastable,  $T_{EW}$ , eutectic temperatures determined for alloy  $A_{inoc}$  have also been drawn as dashed horizontal lines. These reference temperatures are respectively equal to 1165.4 and 1119.4 °C and did not change much with holding time, see Appendix B for their evaluation. Curve A in Fig. 3-a further illustrates that bulk eutectic solidification proceeded with some recalescence before the eutectic plateau was reached. When holding time increased, the records were seen to first flatten and finally present a minimum located in the middle part of the eutectic plateau as clearly seen in

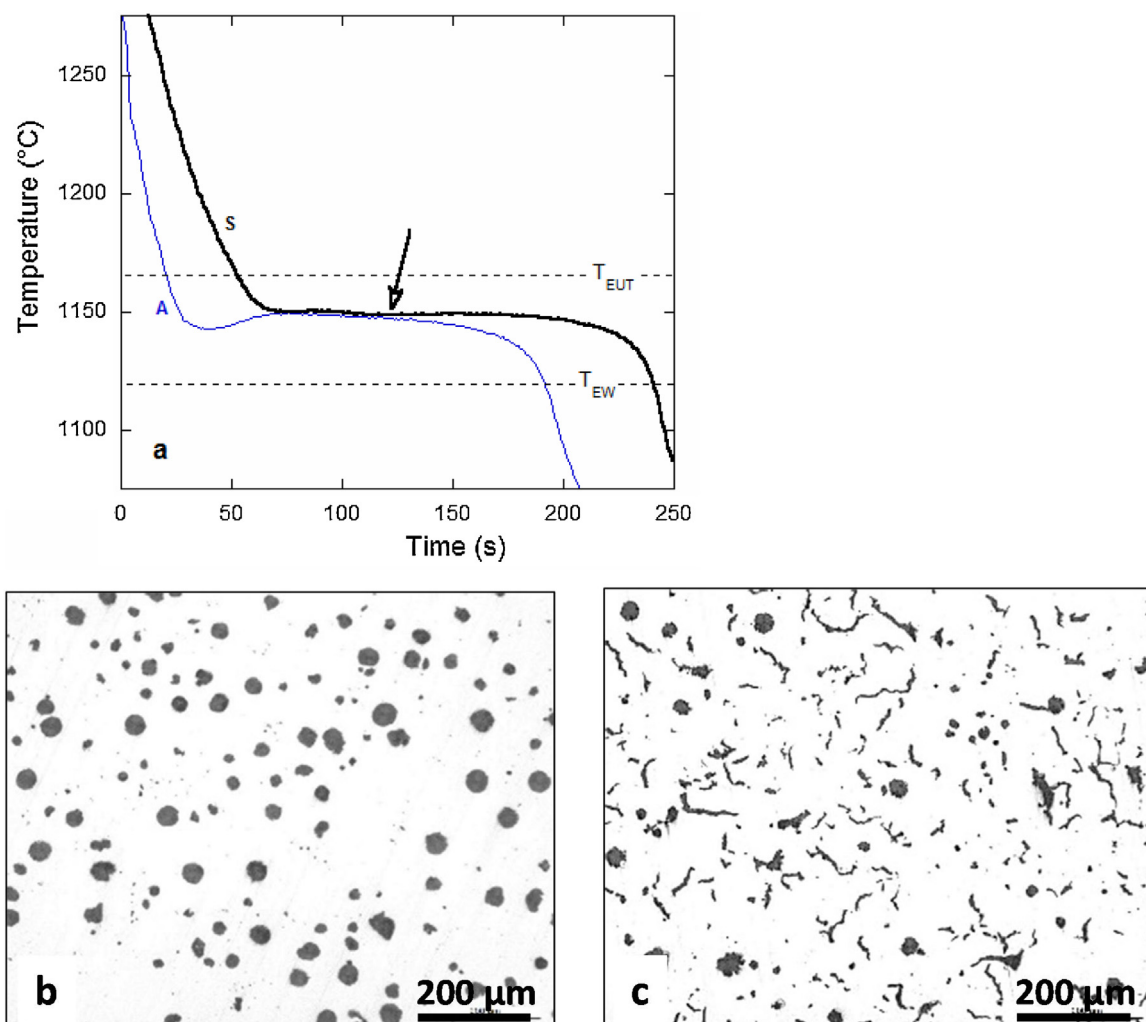


**Fig. 3 – Inoculated samples: cooling curves of trials A and S (a), and micrograph of samples  $A_{inoc}$  (b) and  $S_{inoc}$  (c). The open arrow shows the minimum temperature in the plateau of curve S (see text for details).**

Fig. 3-a for alloy  $S_{inoc}$  (open arrow). This could evidence that the bulk eutectic reaction of inoculated alloys took place in two successive steps, see below.

Typical micrographs of the first ( $A_{inoc}$ ) and last ( $S_{inoc}$ ) samples are shown in Fig. 3-b and c, respectively. They illustrate an evolution from a fully spheroidal graphite iron to a nearly compact one with the holding time due to the decrease in the content of nodularizing elements, see Fig. 1. It should be noted that the small nodules in sample  $A_{inoc}$  have completely disappeared and have been replaced in the  $S_{inoc}$  sample by compact graphite particles. This suggests that the precipitation of graphite in inoculated alloys begins with primary spheroids that give the large nodules that appear with similar size in all inoculated samples. Compact graphite could thus appear later during the bulk eutectic reaction leading, eventually, to the two step plateau observed for alloy  $S_{inoc}$ .

The above qualitative analysis is sustained by the quantitative results illustrated in Fig. 4 where the changes with holding time of the relative area fractions  $f_{III,A}$ ,  $f_{V,A}$  and  $f_{VI,A}$  are reported for the whole set of inoculated samples. It is seen that  $f_{V,A}$ , which could be associated with the large graphite

spheroids, is nearly constant. This thus confirms that these are the small nodules which are progressively replaced with compact graphite. In this series of inoculated alloys, the total graphite fraction,  $f_{graphite}$ , was nearly constant at 0.08–0.10 and no cementite was observed. All microstructure data are collected in Appendix C.

The characteristic temperatures and recalcence for the TA records of inoculated alloys have been plotted in Fig. 5 as function of holding time. It is seen that  $T_{LA}$  and  $T_{E,min}$  remained significantly lower than  $T_{EUT}$  in line with the description of thermal analysis records for hyper-eutectic alloys by Heine [22]. Both  $T_{LA}$  and  $T_{E,min}$  increased with holding time, which is further detailed in Section 4. For the present series of results on inoculated alloys, it is also noticed an overall decrease of the recalcence amplitude. For all samples,  $T_{solidus}$  is above  $T_{EW}$  in agreement with the fact that no cementite was observed for any of the inoculated alloys. Owing to the uncertainty related to the use of the second derivative for evaluating  $T_{solidus}$ , the slight variation of this temperature seen in Fig. 5 may not be significant. The results in Fig. 5 will be discussed further later.



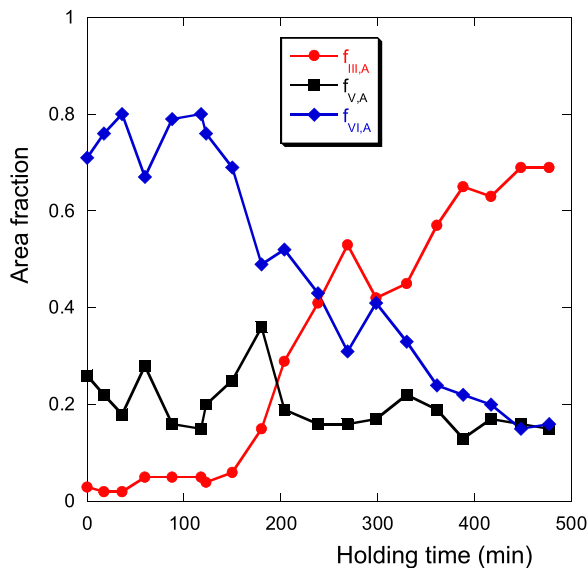


**Fig. 4 – Change with holding time of the relative fractions of graphite,  $f_{III-A}$ ,  $f_{V-A}$  and  $f_{VI-A}$ , for all inoculated samples. After Regordosa et al. [19].**

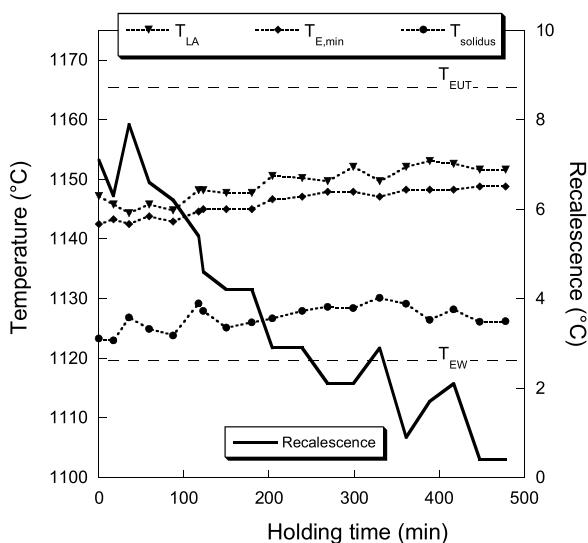


**Fig. 5 – Evolution of the characteristic temperatures and of recalescence during holding for inoculated alloys.**

Fig. 6-a shows the TA records from a few non-inoculated alloys, namely samples  $A_{no-inoc}$ ,  $C_{no-inoc}$  and  $S_{no-inoc}$ . In contrast with the case of inoculated alloys, these records change as a function of holding time. This is in line with the significant microstructure changes observed on the micrographs in Fig. 6-b, c and d. It should be noted that the microstructure of the  $A_{no-inoc}$  sample consists mainly of spheroidal precipitates and that its TA record is similar to those in Fig. 3-a. Solidification of the following non-inoculated samples from B to S occurred in two stages, with a first short plateau at 1139–1149 °C and a main plateau at lower temperature. This latter temperature was observed to decrease with holding time. After Nital etching, samples from  $C_{no-inoc}$  to  $S_{no-inoc}$  did

contain an increasing amount of carbides as illustrated with Fig. 6-e and f.

Quantitative microstructure data are presented in Fig. 7. In Fig. 7-a, the surface fractions of graphite and carbides are plotted as a function of holding time and show the general trend that is expected, namely a decrease in the amount of graphite as cementite is increasingly present. In Fig. 7-b are seen the evolutions of the area fractions of the three types of graphite. During the first 100 min, the amount of types V and VI spheroidal graphite decreases while that of compact graphite significantly increases. At larger holding times, the amounts of the various types of graphite remain nearly constant. Accordingly, the changes seen in the TA curves are due to the decrease of the graphite amount and the associated increase of cementite depicted in Fig. 7-a.

Fig. 8 shows the evolution with holding time of the characteristic temperatures and of recalescence for the non-inoculated samples. It is seen that  $T_{LA}$  increases significantly as in the case of inoculated samples while  $T_{E,min}$  first decreases rapidly during the first 100 min and then more slowly when it takes values below  $T_{EW}$ .  $T_{solidus}$  is below  $T_{EW}$  for all alloys and does not change much with holding time. However, it is worth stressing that no cementite was observed in alloys  $A_{no-inoc}$  and  $B_{no-inoc}$  though  $T_{solidus}$  was below  $T_{EW}$ .

Recalescence first increases as graphite gets more and more compact instead of spheroidal, and it shows a maximum corresponding to alloy  $D_{no-inoc}$ . Such a maximum is in agreement with previous reports [15]. After further holding, recalescence decreases continuously to nearly zero when the structure is mostly white. For alloys  $C_{no-inoc}$  and  $D_{no-inoc}$ ,  $T_{E,min}$  was above  $T_{EW}$ , meaning carbides should have appeared in these samples at the end of solidification. In all following samples,  $T_{E,min}$  was below  $T_{EW}$  so that cementite may have appeared at the beginning of the second plateau or later towards the end of solidification. For samples  $H_{no-inoc}$  to  $S_{no-inoc}$ , the second plateau was entirely located below  $T_{EW}$  and a small but abrupt recalescence could often be observed such as that indicated by the solid arrow in Fig. 2. This thermal arrest could possibly be related to the appearance of ledeburite as discussed elsewhere [23].

## 4. Discussion

Due to the hyper-eutectic composition of the alloys, their solidification began with a primary precipitation of graphite when the temperature dropped below the graphite liquidus. However, this precipitation does not lead to a marked thermal arrest on TA records because the amount of primary graphite remains quite limited even for inoculated alloys [24]. When the temperature decreases further, conditions for austenite formation are finally reached and austenite precipitation begins. This leads to a thermal arrest that has been labelled  $T_{LA}$  in Fig. 2. The values for  $T_{LA}$  for inoculated and non-inoculated alloys are compared in Fig. 9 where have also been plotted the  $T_{E,min}$  values for inoculated alloys and the calculated eutectic temperature,  $T_{EUT}$ .

It is first noticed in Fig. 9 that  $T_{EUT}$  remained nearly constant all along the experiments, in agreement with the fact that the content in silicon of the melt did not change signif-

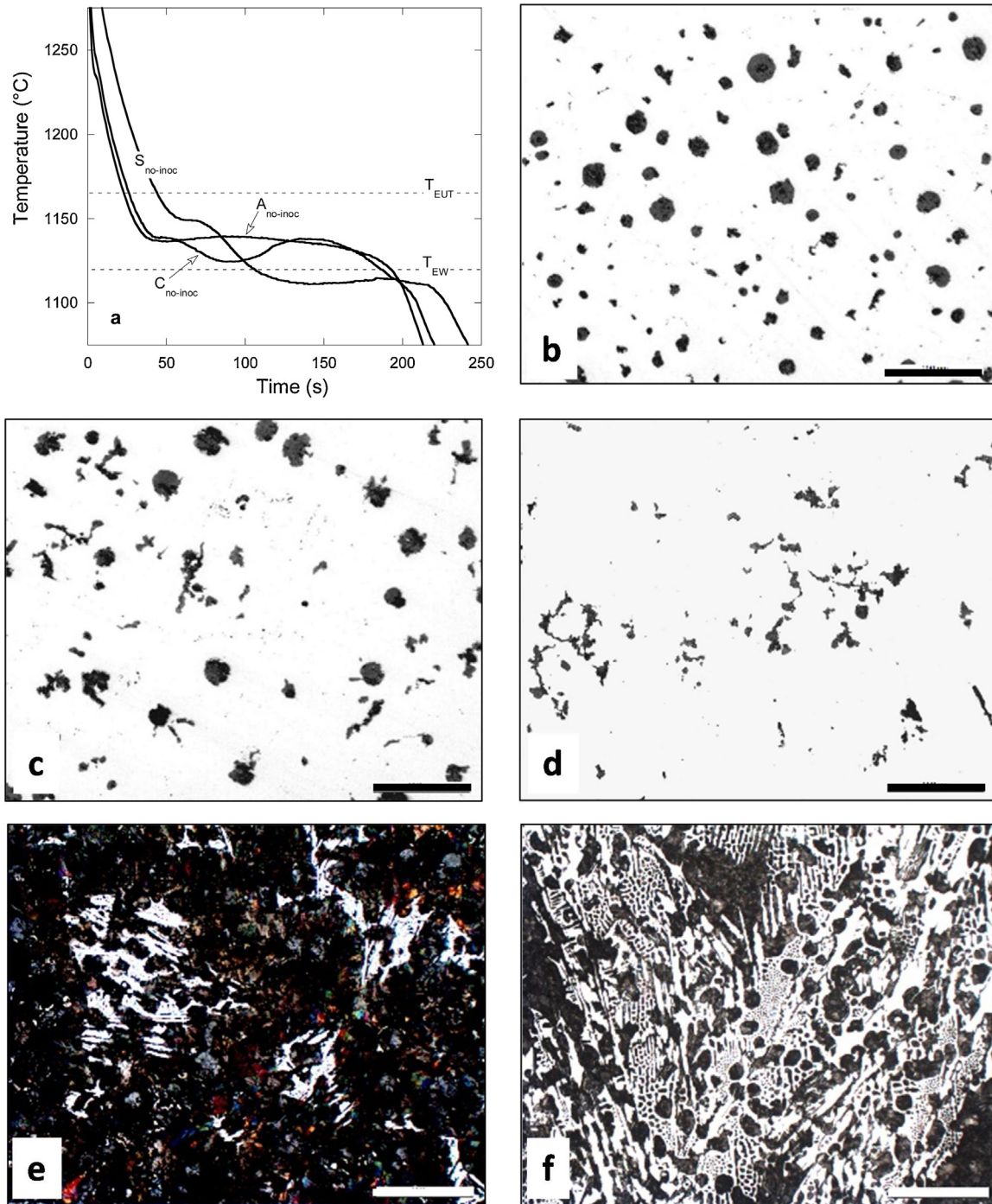


**Fig. 6 – Non-inoculated samples: cooling curves of trials A, C and S (a); micrographs of samples A<sub>no-inoc</sub> (b), C<sub>no-inoc</sub> (c) and S<sub>no-inoc</sub> (d) before etching, and of samples C<sub>no-inoc</sub> (e) and S<sub>no-inoc</sub> (f) after Nital etching. The scale bar is 200  $\mu\text{m}$  long for all micrographs.**

icantly, see Fig. 1 and the calculation formulae in appendix B. Considering the  $T_{LA}$  values, it is thus seen that the liquid was strongly undercooled with respect to the eutectic when austenite started developing at the center of the TA cups, with an undercooling amounting to 20–25 °C at short holding times and more than 10 °C at the end of the experiments. Two reasons related to the present experiments lead to expect the observed increase in  $T_{LA}$  with holding time. These reasons are,

first, the decrease of the alloy carbon content and, second, the decrease of the cooling rate because of the increase in peak temperature.

As a matter of fact, the 0.1 wt.% decrease in the carbon content from the beginning to the end of the trials accounts for about a 10 °C change along the austenite liquidus [22], i.e. it explains most of the change in  $T_{LA}$  recorded for the non-inoculated alloys. The remaining part of the increase of  $T_{LA}$

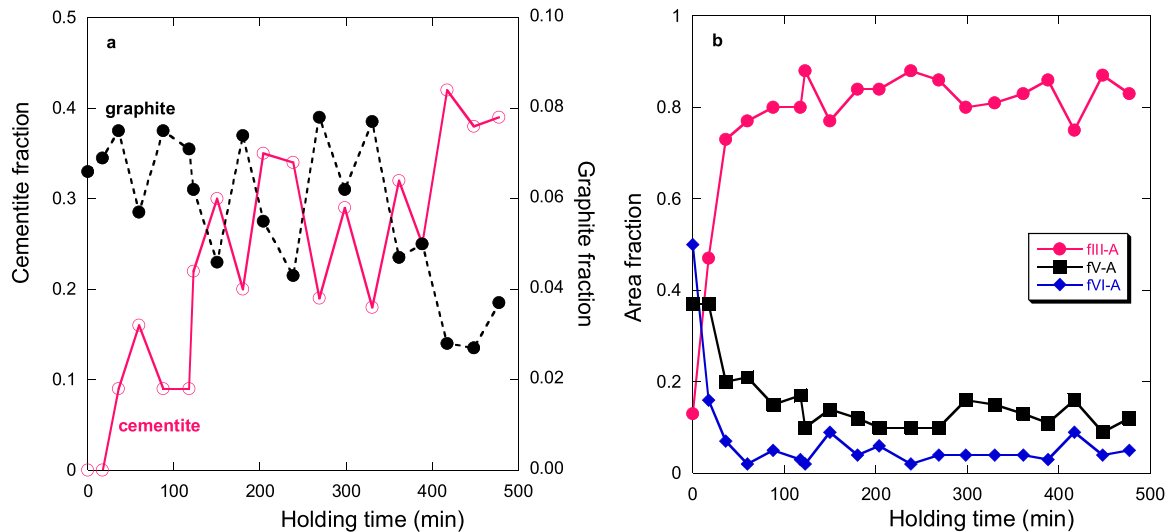


**Fig. 7 – Evolution with holding time of the amount of graphite and cementite (a) and of the relative fractions  $f_{III-A}$ ,  $f_{V-A}$  and  $f_{VI-A}$  (b) in the non-inoculated samples. After Regordosa et al. [19].**

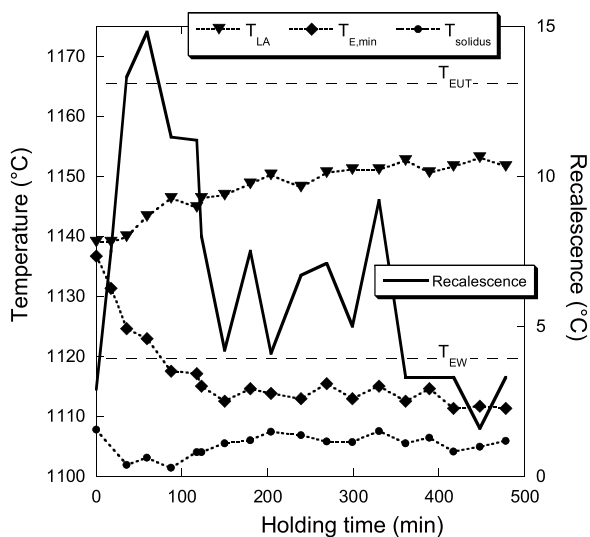


**Fig. 8 – Evolution with holding time of the characteristic temperatures and of recalescence for the non-inoculated samples.**

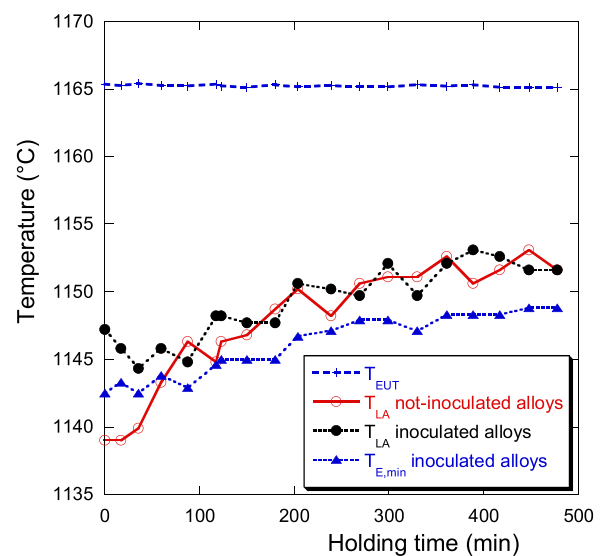


**Fig. 9 – Evolution with holding time of  $T_{EUT}$  (calculated from the non-inoculated alloys' composition), of  $T_{E,min}$  and  $T_{LA}$  for inoculated samples, and of  $T_{LA}$  for non-inoculated samples.**

could possibly be accounted for by the decrease in cooling rate, which gives more time for primary graphite growth, thus moving the solidification path closer to the graphite liquidus and hence increasing the temperature at which austenite may appear.

For inoculated alloys, the  $T_{LA}$  values are significantly higher than those for not-inoculated alloys for short holding times.<sup>1</sup> This difference has certainly to do with the fact that inoculation increases the amount of graphite precipitated during primary solidification, thus overtaking part of the cooling rate

<sup>1</sup> Inoculation leads to an 0.07 wt.% increase in silicon and thus to a 1.6 °C decrease of the austenite liquidus, see Appendix B, which is not considered in the present discussion.

effect again by moving the solidification path closer to the graphite liquidus. At increasing holding time, the solidification path of inoculated alloys during primary precipitation of graphite is thus much less sensitive to change in the carbon content and in the cooling rate as seen with the slower increase in  $T_{LA}$  as compared to non-inoculated alloys.

Finally, part of the difference between  $T_{EUT}$  and  $T_{LA}$  must be related to austenite undercooling as pointed out by Heine [22]. Indeed, calculating the (metastable) austenite liquidus as indicated in Appendix B for the composition of the two extreme alloys A and S gives 1148.0 and 1159.0 °C, respectively. These calculated temperatures are about 10 °C above the measured



$T_{LA}$  temperatures, thus demonstrating austenite undercooling.

Once the extrapolation of the austenite liquidus has been reached, primary precipitates of graphite and austenite may combine to give rise to the eutectic reaction. During this stage, the composition of the liquid is expected to closely follow the austenite liquidus. This may lead to precipitation or dissolution of so-called off-eutectic austenite for any form of graphite, though this has been quantitatively demonstrated only for spheroidal graphite iron [25,26]. The alloy further undercools until  $T_{E,min}$  is reached, which relates to the set-up of bulk eutectic solidification. In the case of inoculated alloys, the  $T_{E,min}$  values in Fig. 9 follow a trend, which nearly parallels that of  $T_{LA}$ . This was expected owing to the fact that the inoculation process was the same all along the experiments. For non-inoculated alloys, the evolution is totally different as discussed below.

The sample  $A_{no-inoc}$  showed the same solidification process as the inoculated alloys characterized by a single eutectic plateau. This suggests that, for this short holding time, there were sufficient exogenous particles remaining in the melt to trigger graphite nucleation when this sample was poured, even without the addition of inoculant. The number of exogenous particles then gradually decreased during melt holding, resulting in a continuous decrease in the number of primary graphite precipitates in the non-inoculated samples, as can be noticed in the micrographs in Fig. 6. This decrease is also associated to a change from spheroidal to compact graphite and to a decrease of  $T_{E,min}$ , which is rapid at first and then slows down when  $T_{E,min}$  is lower than  $T_{EW}$ . Focusing on alloys  $B_{no-inoc}$ ,  $C_{no-inoc}$  and  $D_{no-inoc}$  which all showed a  $T_{E,min}$  value above  $T_{EW}$ , it thus seems that early development of the compact graphite cells is hindered until some high enough undercooling has been reached at which their growth becomes significant and leads to marked recalescence.

The above characteristic of the solidification of CGI as recorded by TA has been stressed since long [15]. It is here associated with a growth hindrance during the early stage of eutectic growth. Some support of this analysis was previously gained by the observation of deep-etched non-inoculated samples [19]. It has been seen that some primary graphite spheroids could evolve in compact graphite cells during the first stage of eutectic solidification, before  $T_{E,min}$  is reached. However, some other spheroids remained growing without developing protuberances that would lead to compact graphite, and thus appeared unchanged until bulk eutectic solidification.

In non-inoculated alloys that showed significant amounts of cementite, it was found that the compact graphite cells show a rounded or an elongated shape. It may easily be concluded that cells appearing round got locked when the metastable eutectic took place, while elongated cells have grown for a while together with ledeburite. This interaction between growth of CG cells and ledeburite could be quantitatively illustrated by recording the number and size of the compact graphite cells. Fig. 10 shows these data as function of holding time. A vertical interrupted line has been added to show when the eutectic plateau started to be entirely below  $T_{EW}$ . It is seen that this transition corresponds to when the size of the cells started to decrease, thus confirming the above

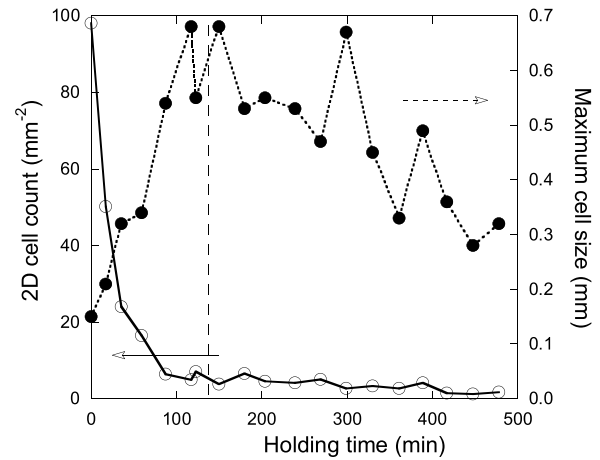


**Fig. 10 – Evolution with holding time of the number and size of compact graphite cells in non-inoculated alloys.**

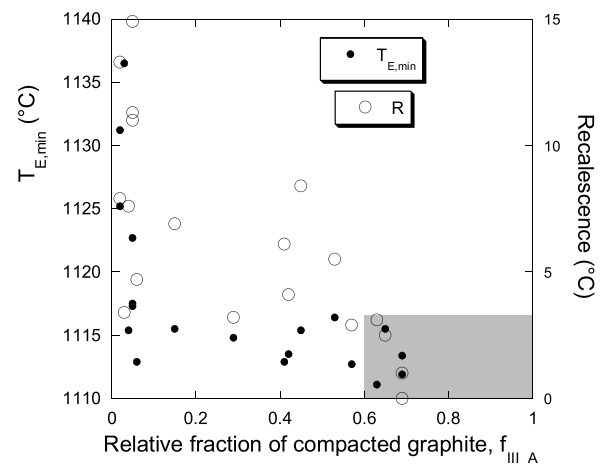


**Fig. 11 – Correlation between the relative amount of compact graphite,  $f_{III,A}$ , in inoculated samples with the values of  $T_{E,min}$  and  $R$  in the corresponding non-inoculated sample. The greyed area corresponds to inoculated alloys with compact graphite.**

schematic. It is worth noting that the size of the cells reported here are quite larger than those measured by Pan et al. [24].

Finally, it is of interest to go back to the question of the capability of thermal analysis as a means to control melt preparation before casting. During holding of the melt, the quantity of nodularizing elements decreases until inoculated alloys solidify mainly as compact graphite while non-inoculated alloys solidify mainly in the metastable system. This suggested to plot the fraction  $f_{III,A}$  of compact graphite in inoculated samples as function of  $T_{E,min}$  and  $R$  measured for the non-inoculated ones. This is done in Fig. 11 where it is seen that inoculated alloys that can be considered as compact graphite iron, i.e. having  $f_{III,A}$  higher than 0.60, refer to the simultaneously lowest values of both  $T_{E,min}$  and  $R$  for the corresponding non-inoculated alloys. These values correspond to a nearly fully metastable solidification. From Fig. 11, it may be inferred that a low inoculation, much lower than that used in

the present study, would give the most appropriate results for characterizing melt preparation for CGI casting.

## 5. Conclusions

A quantitative analysis of both the cooling curves and the microstructure was carried out on thermal analysis samples cast with varying nodularizing content conducting to a change from fully spheroidal to mainly compact graphite. The samples were either or not inoculated leading to very different cooling curves and microstructures for each melt sampling.

For inoculated samples, the changes in the cooling curves were too weak when graphite evolved from spheroidal to compact to be useful for any microstructure prediction or melt control.

On the contrary, non-inoculated samples provided much more information on both microstructure and cooling curve characteristics. For these samples, eutectic solidification takes place with a significant undercooling, which increases as the amount of nodularizer decreases and as graphite changes from spheroidal to compact. This leads to a bulk solidification taking place partly in the metastable system with the formation of carbides.

The results thus obtained on non-inoculated alloys are in line with previous descriptions while providing some more insight through quantitative microstructure analysis, e.g. growth hindrance of compact graphite cells during the first

stage of eutectic growth and competition between compact and white eutectic cells.

The present work provides the whole set of quantitative data necessary for checking the appropriateness of any modelling approach of the solidification of compact graphite cast iron: chemical analysis, cooling curves (in particular minimum eutectic temperature and recalescence) and quantitative microstructure data (amount of phases, number and size of compact eutectic cells).

On a practical point of view, the present work suggests that thermal analysis could certainly be a useful means for control of melt preparation for CGI casting by adding very low level of inoculant in the thermal cups. Experiments in this line are on-going.

## Acknowledgments

The authors would like to thank L. A. Hurtado and Betsaide S.A.L. foundry for all the collaborating efforts made to obtain the samples used in the present work.

## Appendix A.

See [Table A1](#)

**Table A1 – Composition of the 19 alloys, not including the contribution of inoculation (wt.%).**

Alloy	C	Si	Mn	P	S	Cr	Mo	Ni	Cu	Mg	Ti	Ce	La
A	3.75	2.45	0.64	0.022	<0.005	0.049	<0.010	0.027	0.85	0.043	0.021	0.0130	0.0051
B	3.76	2.42	0.63	0.023	<0.005	0.047	<0.010	0.030	0.85	0.040	0.021	0.0130	0.0044
C	3.75	2.45	0.63	0.024	<0.005	0.049	<0.010	0.028	0.85	0.038	0.021	0.0120	0.0037
D	3.74	2.43	0.64	0.022	<0.005	0.050	<0.010	0.028	0.85	0.034	0.021	0.0110	0.0032
E	3.72	2.42	0.63	0.023	<0.005	0.048	<0.010	0.030	0.84	0.035	0.021	0.0100	0.0027
F	3.71	2.45	0.63	0.025	<0.005	0.051	<0.010	0.030	0.84	0.031	0.021	0.0081	0.0021
G	3.72	2.42	0.63	0.022	<0.005	0.049	<0.010	0.030	0.84	0.028	0.021	0.0076	0.0019
H	3.71	2.41	0.64	0.022	<0.005	0.050	<0.010	0.028	0.84	0.021	0.020	0.0070	0.0018
I	3.72	2.44	0.63	0.024	<0.005	0.052	<0.010	0.028	0.84	0.019	0.021	0.0061	0.0015
J	3.69	2.43	0.64	0.023	<0.005	0.054	<0.010	0.028	0.83	0.019	0.021	0.0052	0.0013
K	3.70	2.43	0.62	0.025	<0.005	0.052	<0.010	0.031	0.83	0.018	0.021	0.0047	0.0012
L	3.69	2.43	0.64	0.026	<0.005	0.054	<0.010	0.032	0.83	0.018	0.022	0.0044	0.0011
M	3.67	2.42	0.63	0.021	<0.005	0.051	<0.010	0.026	0.83	0.016	0.020	0.0040	0.0011
N	3.69	2.45	0.63	0.022	<0.005	0.053	<0.010	0.028	0.83	0.015	0.021	0.0036	0.0010
O	3.66	2.43	0.63	0.025	<0.005	0.051	<0.010	0.028	0.83	0.015	0.022	0.0031	0.0009
P	3.67	2.45	0.62	0.025	<0.005	0.050	<0.010	0.028	0.82	0.013	0.022	0.0028	0.0008
Q	3.66	2.40	0.62	0.023	<0.005	0.049	<0.010	0.028	0.83	0.013	0.021	0.0023	0.0007
R	3.67	2.40	0.62	0.023	<0.005	0.049	<0.010	0.027	0.83	0.010	0.021	0.0018	0.0006
S	3.65	2.39	0.62	0.022	<0.005	0.050	<0.010	0.027	0.83	0.008	0.021	0.0014	<0.0005

**Table B1 – Data used to characterize the effect of third elements on the binary Fe-C stable system (according to Castro et al. [20]).**

i species	Solid phases in equilibrium with liquid	w <sub>C</sub>	w <sub>i</sub>	T (°C)	m <sub>i</sub> <sup>γ</sup>	m <sub>i</sub> <sup>g</sup>
Cr	Austenite, graphite and cementite	4.2	4.30	1156	-2.71	13.14
Cu	Austenite and graphite	4.0	3.7	1172	-4.08	40.62
Mn	Austenite, graphite and cementite	4.32	3.0	1139	-5.66	-2.40
Mo	Austenite and graphite	5.0	12.6	1350	-10.3	-4.84
Ni	Austenite and graphite	3.8	10.0	1128	-7.86	18.41
P	Austenite, cementite and Fe <sub>3</sub> P	2.2	7.1	954	-57.8	89.6
Si	Austenite and graphite	3.78	2.0	1162.5	-23.0	113.2

### Appendix B.

In a limited range of silicon content, the austenite and graphite liquidus surfaces could be represented by hyperplanes in the composition space. Accordingly, the austenite liquidus temperature, T<sub>L</sub><sup>γ</sup>, and the graphite liquidus temperature, T<sub>L</sub><sup>g</sup>, could be expressed by linear relations of alloy composition:

$$T_L^\gamma = T_0^\gamma + m_C^\gamma \cdot w_C + \sum_i m_i^\gamma \cdot w_i \quad (B1)$$

$$T_L^g = T_0^g + m_C^g \cdot w_C + \sum_i m_i^g \cdot w_i \quad (B2)$$

in which T<sub>0</sub><sup>γ</sup> and T<sub>0</sub><sup>g</sup> are constants, m<sub>i</sub><sup>γ</sup> and m<sub>i</sub><sup>g</sup> are liquidus slopes relative to element i for austenite and graphite, respectively, and w<sub>i</sub> is the content in element i of the alloy (wt.%).

Using the assessment of the Fe-C system by Gustafson [27], the stable eutectic is given by the invariant point (4.34 wt.% C; 1154 °C). Combining this data with the slope of the austenite and graphite liquidus assessed by Heine [28] leads to the following expressions where the temperature is given in Celsius:

$$T_L^\gamma = 1576.3 - 97.3 \cdot w_C + \sum_i m_i^\gamma \cdot w_i \quad (B3)$$

$$T_L^g = -534.7 + 389.1 \cdot w_C + \sum_i m_i^g \cdot w_i \quad (B4)$$

To estimate the m<sub>i</sub><sup>γ</sup> values, points were selected in the relevant Fe-C-i phase diagrams assessed by Raynor and Rivlin [29] or by Raghavan [30], but the Fe-C-Si system for which the point was taken from a previous assessment of this system [31]. In Table B1 are indicated the selected points and the calculated values of the austenite and graphite liquidus slopes. The expressions derived from this selection are expected to be valid for silicon contents up to 3 wt.% and for any other alloying element up to 1 wt.%.

The intersection of the two hyper-planes describing the austenite and graphite liquidus corresponds to the eutectic trough. Thus, equating Eqs. B3 and B4 gives the eutectic carbon content, w<sub>C</sub><sup>eut</sup>:

$$w_C^{eut} = 4.34 - \frac{\sum_i (m_i^g - m_i^\gamma) \cdot w_i}{m_C^g - m_C^\gamma} \quad (B5)$$

The corresponding eutectic temperature, T<sub>EUT</sub>, is obtained by inserting B5 in either of Eqs. B3 or B4, e.g. B3:

$$T_{EUT} = 1154.02 + \sum_i \left( m_i^\gamma + 97.3 \cdot \frac{m_i^g - m_i^\gamma}{m_C^g - m_C^\gamma} \right) \cdot w_i \quad (B6)$$

For the alloys under investigation which contain silicon, copper and manganese as alloying elements, one gets:

$$T_{EUT} = 1154.02 + 4.246 \cdot w_{Si} + 4.86 \cdot w_{Cu} - 5.00 \cdot w_{Mn} \quad (B7)$$

For the alloys investigated in the present study, one has T<sub>EUT</sub> changing from 1165.1 °C to 1165.4 °C along the series of samples. The calculated metastable eutectic temperature is given as T<sub>W</sub> = 1150 - 12.5 · w<sub>Si</sub> [32], and thus increases slightly from 1119.4 to 1120.1 °C during the series of castings.

Finally, it is worth noting that the carbon equivalent CE of the cast iron is obtained from Eq. B5 as:

$$CE = w_C + \frac{\sum_i (m_i^g - m_i^\gamma) \cdot w_i}{m_C^g - m_C^\gamma} \quad (B8)$$

Using the parameter values listed in Table B1, this expression gives the carbon equivalent noted CE<sub>99</sub> in the main text, Eq. (1). The corresponding expression CE<sub>ASM</sub> suggested in the ASM handbook [21], Eq. (1') in the main text, is due to Neumann [33]. Neumann estimated the coefficients in CE<sub>ASM</sub> using the following two-step procedure: 1. Recording experimental solubility values of carbon in Fe-C-i melts at 1500 °C; 2. Using these values as estimates of the change in carbon content of the binary Fe-C eutectic induced by alloying with element “i”. Hence, the procedure we followed is formerly the same but should give a better estimate of the alloying effect on cast irons because:

- 1 C-i interactions are certainly temperature dependent. The large difference between the eutectic temperature in Fe-C-i systems and the temperature of 1500 °C selected by Neumann may relate to significant changes in the quantitative effect of element “i” on carbon solubility in the liquid.
- 2 The carbon content of the Fe-C eutectic was set at 4.26 wt.% by Neumann while it is now admitted it is 4.34 wt.%.

The difference between the CE<sub>99</sub> and CE<sub>ASM</sub> values illustrated in Fig. 1 is for a large part due to the change in the Fe-C eutectic composition. Further, Fig. 2b in Neumann’s paper

shows that the effect of carbide former elements, e.g. Cr and Mn, on carbon solubility is quite small. Hence, the above shift of the assessed eutectic composition in the binary Fe-C system may well explain that these coefficients are small and negative in  $CE_{ASM}$  while they are small and positive in  $CE_{99}$ .

## Appendix C.

Microstructure data

See [Tables C1 and C2](#)

**Table C1 – Microstructure data for inoculated alloys and maximum recorded temperature,  $T_{peak}$  (°C).**

Sample	$f_{III,C}$	$f_{V,C}$	$f_{VI,C}$	$f_{III,A}$	$f_{V,A}$	$f_{VI,A}$	$f_{graphite}$	$T_{peak}$
A <sub>inoc</sub>	0.07	0.25	0.68	0.03	0.26	0.71	0.091	1282
B <sub>inoc</sub>	0.07	0.23	0.70	0.02	0.22	0.76	0.088	1283
C <sub>inoc</sub>	0.03	0.20	0.77	0.02	0.18	0.80	0.084	1296
D <sub>inoc</sub>	0.07	0.23	0.70	0.05	0.28	0.67	0.082	1294
E <sub>inoc</sub>	0.07	0.14	0.79	0.05	0.16	0.79	0.095	1311
F <sub>inoc</sub>	0.07	0.15	0.78	0.05	0.15	0.80	0.086	1302
G <sub>inoc</sub>	0.06	0.17	0.77	0.04	0.20	0.76	0.086	1313
H <sub>inoc</sub>	0.10	0.20	0.70	0.06	0.25	0.69	0.091	1247
I <sub>inoc</sub>	0.15	0.27	0.58	0.15	0.36	0.49	0.084	1310
J <sub>inoc</sub>	0.25	0.16	0.59	0.29	0.19	0.52	0.086	1307
K <sub>inoc</sub>	0.33	0.13	0.54	0.41	0.16	0.43	0.084	1312
L <sub>inoc</sub>	0.41	0.16	0.43	0.53	0.16	0.31	0.082	1325
M <sub>inoc</sub>	0.35	0.19	0.46	0.42	0.17	0.41	0.084	1333
N <sub>inoc</sub>	0.41	0.21	0.38	0.45	0.22	0.33	0.082	1344
O <sub>inoc</sub>	0.47	0.21	0.32	0.57	0.19	0.24	0.093	1358
P <sub>inoc</sub>	0.46	0.17	0.37	0.65	0.13	0.22	0.094	1346
Q <sub>inoc</sub>	0.54	0.18	0.28	0.63	0.17	0.20	0.088	1367
R <sub>inoc</sub>	0.62	0.19	0.19	0.69	0.16	0.15	0.091	1357
S <sub>inoc</sub>	0.63	0.18	0.19	0.69	0.15	0.16	0.087	1367

**Table C2 – Microstructure data for non-inoculated alloys and maximum recorded temperature,  $T_{peak}$  (°C).**

Sample	$f_{III,C}$	$f_{V,C}$	$f_{VI,C}$	$f_{III,A}$	$f_{V,A}$	$f_{VI,A}$	$f_{carbides}$	$f_{graphite}$	$D_{Cell}(mm)$	$N_{Cell}(mm^{-2})$	$T_{peak}$
A <sub>no-inoc</sub>	0.15	0.35	0.50	0.13	0.37	0.50	0.00	0.066	0.15	98.06	1283
B <sub>no-inoc</sub>	0.42	0.36	0.22	0.47	0.37	0.16	0.00	0.069	0.21	50.16	1291
C <sub>no-inoc</sub>	0.54	0.27	0.19	0.73	0.20	0.07	0.09	0.075	0.32	24.01	1290
D <sub>no-inoc</sub>	0.65	0.28	0.08	0.77	0.21	0.02	0.16	0.057	0.34	16.46	1298
E <sub>no-inoc</sub>	0.63	0.22	0.15	0.80	0.15	0.05	0.09	0.075	0.54	6.38	1294
F <sub>no-inoc</sub>	0.64	0.23	0.13	0.80	0.17	0.03	0.09	0.071	0.68	4.97	1299
G <sub>no-inoc</sub>	0.67	0.19	0.14	0.88	0.10	0.02	0.22	0.062	0.55	7.08	1308
H <sub>no-inoc</sub>	0.40	0.20	0.40	0.77	0.14	0.09	0.30	0.046	0.68	3.80	1294
I <sub>no-inoc</sub>	0.60	0.24	0.16	0.84	0.12	0.04	0.20	0.074	0.53	6.64	1303
J <sub>no-inoc</sub>	0.58	0.21	0.21	0.84	0.10	0.06	0.35	0.055	0.55	4.58	1290
K <sub>no-inoc</sub>	0.69	0.19	0.11	0.88	0.10	0.02	0.34	0.043	0.53	4.11	1300
L <sub>no-inoc</sub>	0.62	0.18	0.20	0.86	0.10	0.04	0.19	0.078	0.47	5.03	1310
M <sub>no-inoc</sub>	0.57	0.26	0.17	0.80	0.16	0.04	0.29	0.062	0.67	2.73	1321
N <sub>no-inoc</sub>	0.64	0.20	0.17	0.81	0.15	0.04	0.18	0.077	0.45	3.36	1328
O <sub>no-inoc</sub>	0.58	0.23	0.19	0.83	0.13	0.04	0.32	0.047	0.33	2.73	1337
P <sub>no-inoc</sub>	0.60	0.22	0.18	0.86	0.11	0.03	0.25	0.050	0.49	4.11	1334
Q <sub>no-inoc</sub>	0.43	0.22	0.35	0.75	0.16	0.09	0.42	0.028	0.36	1.46	1348
R <sub>no-inoc</sub>	0.47	0.22	0.30	0.87	0.09	0.04	0.38	0.027	0.28	1.22	1338
S <sub>no-inoc</sub>	0.59	0.23	0.18	0.83	0.12	0.05	0.39	0.037	0.32	1.77	1346



## REFERENCES

- [1] Dawson S, Schroeder T. Practical applications for compacted graphite iron. *AFS Trans* 2004;112, paper 04-047.
- [2] König M, Wessén M. Influence of alloying elements on microstructure and mechanical properties of CGI. *Int J Cast Met Res* 2010;23:97–110.
- [3] Bazdar M, Abbasi HR, Yaghtin AH, Rassizadehghani J. Effect of sulfur on graphite aspect ratio and tensile properties in compacted graphite irons. *J Mater Proc Tech* 2009;209:1701–5.
- [4] Charoenvilaisiri S, Stefanescu DM, Ruxanda R, Piwonka TS. Thin wall compacted graphite iron castings. *AFS Trans* 2002;110, paper 02-176.
- [5] Lekakh SN, Qing J, Richards VL. Investigation of vast iron processing to produce controlled dual graphite structure in casting. *AFS Trans* 2012;120:297–306.
- [6] Gorny M, Kawalec M. Effects of titanium addition on microstructure and mechanical properties of thin-walled compacted graphite iron castings. *JMEPEG* 2013;22:1519–24.
- [7] Firican MC, Riposan I. Graphite phase characteristics in compacted/vermicular graphite cast iron inoculated in the mould. *Adv Mater Res* 2015;1128:72–9.
- [8] Loizaga A, Larrañaga P, Asenjo I, Sertucha J, Suárez R. An experimental methodology based on solidification curves for controlling the manufacture of compacted graphite irons. *AFS Trans* 2012;120, paper 12-006.
- [9] Gorny M. Cast iron: compacted graphite. In: *Encyclopedia of iron, steel, and their alloys*. Taylor and Francis; 2015. p. 718–34.
- [10] Mampaey F, Habets D, Plessers J, Seutens F. Online oxygen activity measurements to determine optimal graphite form during compacted graphite iron production. *Int J Met* 2010;42:25–40.
- [11] Dawson S. Controlling the production of compacted graphite iron. *Modern Casting* 1998;88:38–41.
- [12] Stefanescu DM, Martínez F, Chen IG. Solidification behaviour of hypoeutectic and eutectic graphite cast irons. Chilling tendency and eutectic cells. *AFS Trans* 1983;91: 205–16.
- [13] Jinhai Liu, Litao Yi, Guolu Li, Changqi Liu, Yinguo Li, Zhaoyu Yang. Influence of fading on characteristics of thermal analysis curve of compacted graphite iron. *China Foundry* 2011;8:295–9.
- [14] Backerud L, Nilsson K, Steen M. Study of nucleation and growth of graphite in magnesium-treated cast iron by means of thermal analysis. In: *The metallurgy of cast Iron*. Georgi Pub. Co.; 1975. p. 625–37.
- [15] Stefanescu DM, Loper CR, Voigt RC, Chen IG. Cooling curve structure analysis of compacted/vermicular graphite cast irons produced by different melt treatments. *AFS Trans* 1982;90:333–48.
- [16] Rodriguez S, Castro M, Herrera M, Mendez J, Escalante JI, Gonzalez C. Thermal analysis of compacted graphite cast irons containing various levels of Mg and S. *Int J Cast Met Res* 1999;11:381–6.
- [17] Sun XJ, Li YX, Chen X. Identification and evaluation of modification level for compacted graphite cast iron. *J Mater Process Technol* 2008;200:471–80.
- [18] Hernando JC, Domeij B, Gonzalez D, Amieva JM, Dioszegi A. New experimental technique for nodularity and Mg fading control in compacted graphite iron production on laboratory scale. *Metall Mater Trans A* 2017;48A:5432–41.
- [19] Regordosa A, de la Torre U, Loizaga A, Sertucha J, Lacaze J. Microstructure changes during solidification of cast irons – effect of chemical composition and inoculation on competitive spheroidal and compacted graphite growth. *Int J Met* 2020;14:681–8.
- [20] Castro M, Herrera M, Cisneros MM, Lesoult G, Lacaze J. Simulation of thermal analysis applied to the description of the solidification of hypereutectic SG cast irons. *Int J Cast Met Res* 1999;11:369–74.
- [21] Stefanescu DM, Lacaze J. Thermodynamics principles as applied to cast iron. In: *ASM handbook, volume 1A, Cast iron science and technology*. ASM International; 2017. p. 31–42.
- [22] Heine RW. Austenite liquidus, carbide eutectic and undercooling in process control of ductile base iron. *AFS Trans* 1995;103:199–206.
- [23] Lacaze J, Regordosa A, Sertucha J. Quantitative analysis of the effect of inoculation and magnesium content on compacted graphite irons – a modelling approach. Work in progress.
- [24] Pan EN, Ogi K, Loper CR. Analysis of the solidification process of compacted/vermicular graphite cast iron. *AFS Trans* 1982;90:509–27.
- [25] Lesoult G, Castro M, Lacaze J. Solidification of spheroidal graphite cast iron. Part I: physical modelling. *Acta Mater* 1998;46:983–95.
- [26] Lacaze J, Lesoult G, Castro M. Solidification of spheroidal graphite cast iron. Part II: numerical simulation. *Acta Mater* 1998;46:997–1010.
- [27] Gustafson PA. A thermodynamic evaluation of the Fe-C system. *Scand J Metall* 1985;14:259–67.
- [28] Heine RW. The Fe-C-Si solidification diagram for cast irons. *AFS Trans* 1986;94:391–402.
- [29] Raynor GV, Rivlin VG. Phase equilibria in iron ternary systems. The Institute of Metals; 1988.
- [30] Raghavan V. Phase diagrams of ternary iron alloys. The Indian Institute of Metals; 1987.
- [31] Lacaze J, Sundman B. An assessment of the Fe-C-Si system. *Metall Trans* 1991;22A:2211–23.
- [32] Lacaze J. Solidification of spheroidal graphite cast irons. Part III: microsegregation related effects. *Acta Mater* 1999;47:3779–92.
- [33] Neumann F. The influence of additional elements on the physico-chemical behavior of carbon in carbon saturated molten iron. In: *The American Society of Metals, organizer. Proceedings of recent research on cast iron, Detroit, 1964 June 16–18*. Gordon and Breach; 1968. p. 659–705.